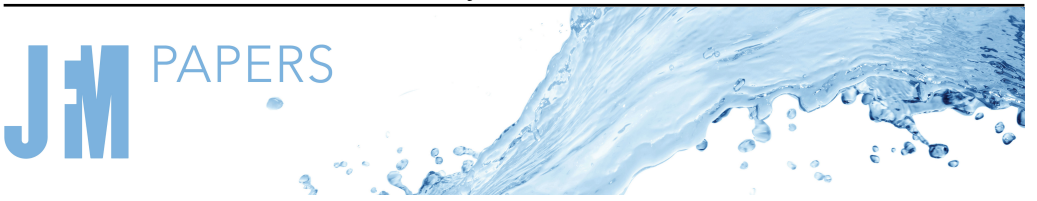
J. Fluid Mech. (2025), *vol.* 1023, A28, doi:10.1017/jfm.2025.10838



Influence of ambient temperature on cavitation bubble dynamics

Shaocong Pei[1,2], **A-Man Zhang**[1,2,4], **Chang Liu**[1,2], **Tianyuan Zhang**[1,2], **Rui Han**[3] and **Shuai Li**[1,2,4]

[1]College of Shipbuilding Engineering, Harbin Engineering University, Harbin 150001, PR China

[2]National Key Laboratory of Ship Structural Safety, Harbin Engineering University, Harbin 150001, PR China

[3]Heilongjiang Provincial Key Laboratory of Nuclear Power System and Equipment, Harbin Engineering University, Harbin 150001, PR China

[4]Nanhai Institute of Harbin Engineering University, Sanya 572024, PR China

Corresponding authors: Shuai Li, lishuai@hrbeu.edu.cn; A-Man Zhang, zhangaman@hrbeu.edu.cn

(Received 27 May 2025; revised 13 October 2025; accepted 14 October 2025)

We examine how ambient temperature T (23–90 °C) alters the dynamics of spark-induced cavitation bubbles across a range of discharge energies. As T rises, the collapse of an isolated spherical bubble weakens monotonically, as quantified by the Rayleigh collapse factor, minimum volume and maximum collapse velocity. When the bubble is generated near a rigid wall, the same thermal attenuation is reflected in reduced jet speed and diminished migration. Most notably, at $T \gtrsim 70$ °C, we observe a previously unreported phenomenon: secondary cavitation nuclei appear adjacent to the primary bubble interface where the local pressure falls below the Blake threshold. The pressure reduction is produced by the over-expansion of the primary bubble itself, not by rarefaction waves as suggested in earlier work. Coalescence between these secondary nuclei and the parent bubble seeds pronounced surface wrinkles that intensify Rayleigh–Taylor instability and promote fission, providing an additional route for collapse strength attenuation. These findings clarify the inception mechanism of high-temperature cavitation and offer physical insight into erosion mitigation in heated liquids.

Key words: bubble dynamics, cavitation

© The Author(s), 2025. Published by Cambridge University Press. This is an Open Access article, distributed under the terms of the Creative Commons Attribution licence (https://creativecommons.org/licenses/by/4.0/), which permits unrestricted re-use, distribution and reproduction, provided the original article is properly cited.

https://doi.org/10.1017/jfm.2025.10838 Published online by Cambridge University Press

1. Introduction

The temperature-dependent dynamics of cavitation bubbles has recently garnered significant research interest. This phenomenon not only is crucial in industrial applications, such as the erosion mitigation in high-temperature fluid machinery (Plesset 1972; Phan *et al.* 2022), structural vibrations caused by cavitation in spacecraft propulsion systems (Dular & Petkovšek 2018; Wei *et al.* 2022) and pulsed laser ablation techniques for tuning nanomaterial properties (Takada, Nakano & Sasaki 2010; Wu *et al.* 2021), but also plays a pivotal role in fundamental scientific studies, including sonoluminescence (Putterman & Weninger 2000; Brenner, Hilgenfeldt & Lohse 2002) and bubble nucleation at high temperatures (Caupin & Herbert 2006; Seddon *et al.* 2011). Understanding how ambient temperature affects cavitation bubble dynamics is essential for addressing the aforementioned complex challenges.

Among the challenges in bubble dynamics, the fundamental mechanisms and mitigation of cavitation erosion remain an intense and active research focus. Extensive investigations have characterised the shock waves (Supponen *et al.* 2017; Reuter, Deiter & Ohl 2022), microjets (Supponen *et al.* 2016; Lechner *et al.* 2019) and thermal loading (Dular & Coutier-Delgosha 2013; Beig, Aboulhasanzadeh & Johnsen 2018) generated during bubble collapse. In contrast, the role of ambient temperature in modulating cavitation bubble dynamics has received comparatively little attention. Limited erosion studies employing standardised specimens reveal a pronounced temperature dependence, with peak damage occurring at moderate water temperatures (Plesset 1972; Dular 2016). Although these observations establish a clear link between temperature and cavitation aggressiveness, the underlying physical mechanisms remain poorly understood, underscoring the need for a fundamental investigation at the single-bubble perspective.

Unlike other liquid properties, such as viscosity (Reese *et al.* 2022), surface tension (Wu *et al.* 2021; Han *et al.* 2022), compressibility (Keller & Miksis 1980; Wang 2016; Han, Yan & Li 2024) and gas saturation (Brenner *et al.* 2002; Preso *et al.* 2024*a*), the ambient temperature chiefly modifies the internal vapour pressure and governs heat and mass transfer at the bubble interface (Phan *et al.* 2022; Zhang *et al.* 2024). For example, laser-induced bubbles in water exhibit a pronounced dependence of oscillation period on ambient temperature (Barbaglia & Bonetto 2004). In a more striking demonstration, a spark-induced cavitation bubble initiated in liquid nitrogen at $-199\,^{\circ}\mathrm{C}$ does not collapse violently; instead, it executes low-amplitude pulsations around an enlarged equilibrium radius while displaying intense interfacial instabilities (Chen *et al.* 2024). Numerical simulations by Phan *et al.* (2022) corroborate these observations, showing that higher temperatures raise the vapour pressure, suppress condensation, and consequently attenuate the peak pressure reached at minimum bubble volume. Recently, Geng *et al.* (2025) quantified the temperature dependence of spark-generated bubbles using the Keller model incorporating heat transfer, phase change and compressibility. They attributed this high-temperature suppression to a dramatic drop in peak vapour condensation rate from 30 to $95\,^{\circ}\mathrm{C}$. While these findings establish that elevated temperature mitigates bubble collapse, a systematic characterisation and a mechanistic explanation remain elusive. Crucially, how this temperature dependence manifests in near-wall configurations, where bubble dynamics is inherently non-spherical, remains an open and critical question.

In this study, we conducted over four hundred spark-generated cavitation bubble experiments in the free field and adjacent to a rigid wall. The extensive dataset clarifies the thermodynamics during bubble expansion, quantifies the systematic attenuation of bubble collapse, and extends the analysis to elucidate how temperature governs bubble jetting and

https://doi.org/10.1017/jfm.2025.10838 Published online by Cambridge University Press

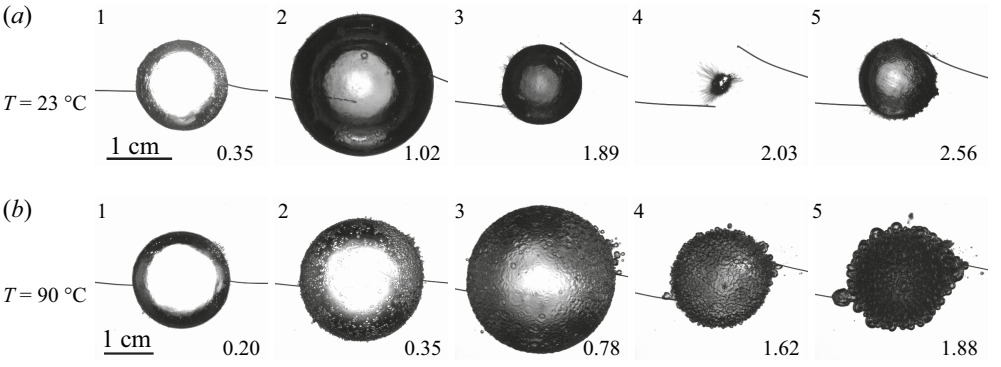


Figure 1. Representative high-speed images of spark-generated bubbles in a free field. (*a*) At $T = 23\,^{\circ}\mathrm{C}$, the bubble remains nearly spherical with a smooth surface during expansion, collapse and rebound. (*b*) At $T = 90^{\circ}\mathrm{C}$, the interface remains smooth during early expansion ($t = 0.2$), then secondary cavitation bubbles emerge around the bubble ($t = 0.35$). These secondary cavitation bubbles coalesce into the main bubble while it is still growing ($t = 0.78$), creating surface wrinkles that intensify during collapse ($t = 1.62$). Upon rebound, the wrinkles develop into pronounced Rayleigh–Taylor instabilities ($t = 1.88$). The time displayed in the lower right corner is normalised by characteristic collapse time, $R_{max}\sqrt{\rho/(P_\infty - P_v)}$, where R_{max} is the maximum bubble radius, ρ the liquid density, P_∞ the hydrostatic pressure at infinity, and P_v the saturated vapour pressure; the resulting values are 1.11 and 2.60 ms, respectively.

migration near a rigid boundary. Remarkably, we identify a novel physical phenomenon in our experiments: when $T \gtrsim 70\,^{\circ}\mathrm{C}$, secondary cavitation forms near the bubble surface during the expansion phase, followed by coalescence-induced surface wrinkles. These perturbations enhance Rayleigh–Taylor instability and contribute to bubble fission, as shown in figure 1. In contrast, experiments conducted at lower temperatures do not exhibit this phenomenon. We employ Blake's criterion to determine the origin of secondary cavitation, verify it by estimating the minimum bubble pressure, and further investigate the role of discharge energy in modulating its onset. In contrast to earlier mechanisms invoking rarefaction waves (Supponen *et al.* 2017; Horiba, Ogasawara & Takahira 2020; Rosselló *et al.* 2023), the phenomenon documented here is governed primarily by elevated ambient temperature and the intrinsic bubble dynamics. These findings advance the fundamental understanding of thermally mediated cavitation inception and suggest a new route for mitigating cavitation erosion.

The work is structured as follows. Section 2 details the experimental set-up and presents a concise yet robust method for estimating the minimum bubble pressure. Section 3 examines bubble-collapse patterns in a free field, supported by theoretical analysis using the Keller equation. Section 4 identifies the mechanism of secondary cavitation and quantifies the influence of ambient temperature and discharge energy on its inception. Section 5 turns to non-spherical bubble dynamics adjacent to a rigid wall, elucidating the fundamental processes relevant to cavitation erosion and complemented by a weakly compressible boundary integral simulation. Finally, the main conclusions are drawn in § 6.

2. Methodology

2.1. *Experimental set-up*

In this study, cavitation bubbles were generated using an underwater low-voltage electric discharge technique (Turangan *et al.* 2006; Cui *et al.* 2018; Han *et al.* 2022) under controlled ambient temperature conditions. The experimental set-up, illustrated schematically in figure 2, comprises two primary subsystems: a discharge system and

https://doi.org/10.1017/jfm.2025.10838 Published online by Cambridge University Press

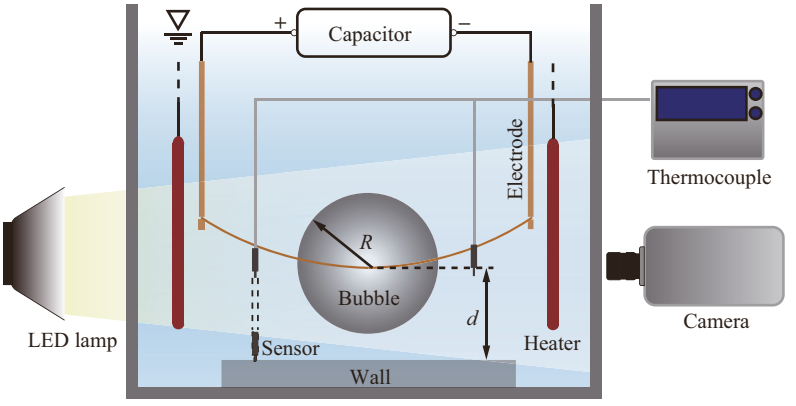


Figure 2. Experimental set-up for cavitation bubble dynamics in various ambient temperatures. The bubble is generated by a underwater low-voltage electric discharge method. The temperature of the water is controlled by two resistance-type heaters arranged symmetrically.

a heating system. A 500 μF capacitor was employed as the power source. To localise bubble formation, a defect was intentionally introduced at the midpoint of the wire (Zhang *et al.* 2024), increasing local resistance and enabling bubble generation through intense Joule heating at the defect site during discharge. To ensure statistical reliability and reproducibility, the experiment was repeated at least 15 times for each temperature.

Experiments were conducted in a transparent tempered-glass water tank with dimensions of 350 mm × 350 mm × 350 mm and a wall thickness of 5 mm. A Polymethyl Methacrylate plate, measuring 300 mm × 300 mm × 30 mm, was fixed at the bottom of the tank to provide a rigid-wall boundary condition. The tank was filled with deionised water to a depth of 300 mm and left to stand in the test tank for at least 12 h before experiments, ensuring it was visibly bubble-free during the tests. Two resistance-type heaters (20 Ω) were used to precisely regulate the water temperature from 23 to 90 °C. Temperatures were measured using two K-type thermocouples (TASI, TA612C) positioned approximately 50 mm from the bubble centre. Within a 100 mm radius surrounding the bubble, spatial temperature variations were kept to a maximum of 0.5 °C. Atmospheric pressure was monitored using a digital pressure gauge (LANGFAN, XY-3041). To capture the transient behaviours of the cavitation bubble, a high-speed camera (Phantom, V2012) equipped with a macro lens (LAOWA 100 mm F2.8) is triggered simultaneously with the discharge. Illumination is provided by a 2000 W strobe-free LED lamp, which is diffused through matt glass to achieve uniform backlighting. The camera operates at 45 000−67 000 frames per second with the exposure time of 1 μs. The bubble radius $R(t)$ in our experiment is determined using the volume equivalence method, expressed as $R(t) = \sqrt[3]{3V_b(t)/(4\pi)}$ (Zeng *et al.* 2018), where $V_b(t)$ represents the time-dependent bubble volume and is obtained by integrating the bubble profile. The uncertainty in the length measurement corresponds to a single pixel, which is approximately 0.07 mm (approximately 0.5 % of R_{max}).

2.2. *Pressure estimation within cavitation bubbles*

We estimate the bubble internal minimum pressure at the point of bubble maximum expansion, P_{min}, from the bubble motion equation, together with the experimentally measured velocity and acceleration of the bubble surface. Specifically, the Keller equation (Keller & Miksis 1980) describes the dynamic behaviour of an initially spherical bubble

https://doi.org/10.1017/jfm.2025.10838 Published online by Cambridge University Press

oscillating in an unbounded field:

$$\left(1-\frac{\dot{R}}{c_\infty}\right)R\ddot{R}+\frac{3}{2}\left(1-\frac{\dot{R}}{3c_\infty}\right)\dot{R}^2=\left(1+\frac{\dot{R}}{c_\infty}\right)\frac{P_l-P_\infty}{\rho}+\frac{\dot{P}_l R}{\rho c_\infty}, \tag{2.1}$$

where R denotes the bubble radius, c_∞ the speed of sound, ρ the liquid density and P_∞ the hydrostatic pressure at infinity. The liquid pressure at the bubble surface, P_l, is given by

$$P_l=P_b-\frac{2\sigma}{R}-\frac{4\mu\dot{R}}{R}, \tag{2.2}$$

where P_b is the pressure inside the bubble, σ the surface tension and μ the dynamic viscosity, respectively. Several simplifications can be made. When estimating the minimum pressure corresponding to the moment of maximum expansion, the Mach number $\dot{R}/c_\infty$ is negligibly small in the time interval around that moment, allowing us to disregard the compressibility of the liquid. Viscosity can also be neglected because the shear rate vanishes. In addition, surface tension is safely ignored for the centimetre-sized spark-generated bubbles in this study (Han *et al.* 2022). Furthermore, we examine the Péclet numbers for heat and mass transport:

$$Pe_h=\frac{U R_{max}}{\alpha}\sim O(10^5),\ Pe_m=\frac{U R_{max}}{D}\sim O(10^7), \tag{2.3}$$

where α and D denote the thermal and mass diffusivities, respectively. The characteristic velocity is taken as $U=\sqrt{(P_\infty-P_v)/\rho}$. The large Péclet numbers, $Pe_h\sim O(10^5)$ and $Pe_m\sim O(10^7)$, suggest that both heat and mass diffusion are negligible during the bubble oscillation in our experimental system. By rearranging (2.1) and (2.2), the minimum pressure within the bubble can be described as

$$P_{min}=P_\infty+\rho(R\ddot{R})|_{R=R_{max}}. \tag{2.4}$$

The maximum bubble radius, R_{max}, can be directly measured from experiments, while the acceleration term, $\ddot{R}$, can be derived from the temporal evolution of the bubble radius. To achieve this, we fit the bubble radius over a time interval encompassing the maximum radius using a cubic polynomial. By calculating the second derivative of this polynomial with respect to time, one can obtain $\ddot{R}$. A similar method has been applied for building thermal models of one-dimensional cavitation bubbles in microtubes (Sun *et al.* 2009). The chosen time interval for radius fitting is 0.25 times the first period of the bubble. This interval strikes a balance between incorporating enough experimental data for a reliable fit and keeping the period short to enhance accuracy. More details about the uncertainty method can be found in Appendix A.

3. Spherical bubble dynamics

In this section, we begin by presenting the general physical phenomena of spark-generated cavitation bubbles in a free field under varying ambient temperatures. We then employ a pressure–temperature phase diagram to interpret the temperature-dependent variations in maximum bubble radius. To broaden the applicability of our conclusions, we use the maximum bubble radius R_{max}, the difference between the hydrostatic pressure and the saturated vapour pressure $\Delta P=P_\infty-P_v$, and the liquid density ρ as basic quantities to convert other parameters into non-dimensional quantities. Finally, within this non-dimensional framework, we provide a quantitative analysis of key bubble-collapse

https://doi.org/10.1017/jfm.2025.10838 Published online by Cambridge University Press

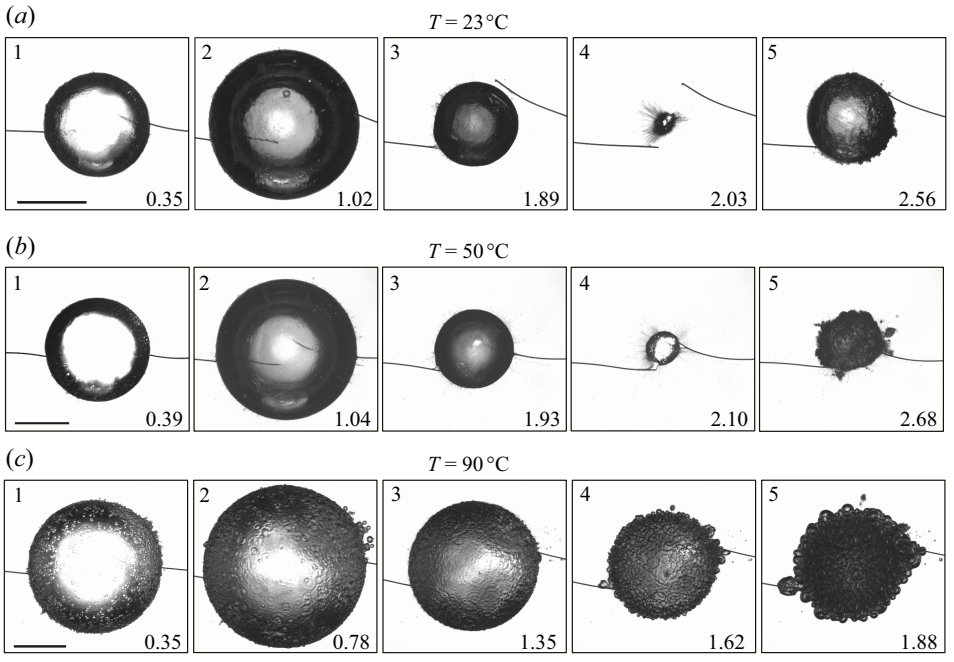


Figure 3. Three representative experiments conducted in the free field at different ambient temperatures. (*a*) The bubble was initiated at room temperature (23 °C), maintaining a spherical shape throughout the oscillation process. (*b*) The bubble was initiated at 50 °C. Its contraction intensity is weakened. (*c*) The bubble was initiated at 90 °C. During the expansion stage, secondary cavitation occurs near the bubble wall. During the collapse stage, the intensity of bubble contraction is further weakened, and fission occurs in the rebound process. Normalised times are indicated in the lower-right corners of each frame. The time scales for non-dimensionalisation ($R_{max}\sqrt{\rho/(P_\infty - P_v)}$) are 1.11, 1.38 and 2.60 ms, respectively. Here P_v is the saturated vapour pressure corresponding to the ambient temperature. The length of horizontal line indicated in the lower-left corner of the first frame is 10 mm.

behaviours, including maximum bubble radius, bubble-collapse time and maximum bubble-collapse velocity.

3.1. *Experimental observations*

We conducted extensive experiments under the ambient temperature range of 23–90 °C in the free field. The results from three representative experiments, each conducted at different ambient temperatures T, are illustrated in figure 3(*a–c*). Figure 3(*a*) shows the expansion (frames 1–2), collapse (frames 3–4) and rebound (frame 5) of a bubble at room temperature ($T = 23$ °C). The bubble maintains nearly spherical oscillations, with a maximum radius of 11.4 mm, collapsing to a non-dimensional minimum radius R_{min}/R_{max} of approximately 0.14. Using the method described in § 2.2, we determined the minimum pressure inside the bubble (at the non-dimensional time $t \approx 1.02$) to be approximately 11 000 Pa.

Figure 3(*b*) illustrates representative moments from the experiment conducted at $T =$ 50 °C, and the corresponding saturated vapour pressure is approximately 12 000 Pa. Compared with the room temperature experiment under the same discharge voltage (figure 3*a*), the maximum bubble radius R_{max} increases to approximately 13.1 mm (frame 2). Subsequently, the bubble undergoes a spherical collapse with lower intensity, retaining a normalised minimum radius R_{min}/R_{max} of approximately 0.19 at the end of the first collapse phase (frame 4). Notably, during the rebound phase, the bubble deviates from

https://doi.org/10.1017/jfm.2025.10838 Published online by Cambridge University Press

a spherical shape due to the influence of Rayleigh–Taylor instability (Frost & Sturtevant 1986; Brennen 2002), which results in a rough and opaque surface of the bubble (frame 5). The estimated minimum pressure inside the bubble is approximately 21 000 Pa, which is approximately twice that in the first experiment.

Figure 3(*c*) shows representative bubble behaviours observed in the experiment conducted at $T = 90\,^{\circ}\mathrm{C}$. Compared with the previous two cases, the bubble expands to a larger maximum radius of 15.5 mm (frame 2). Additionally, the collapse of the bubble is further weakened: it reaches its minimum volume earlier, and the normalised minimum radius R_{min}/R_{max} is as large as 0.65 (frame 4). An interesting phenomenon occurs during the expansion phase: microbubbles, approximately 0.1 mm in diameter, nucleate explosively near the bubble surface (frame 2), forming a series of secondary cavitation bubbles. These secondary bubbles then migrate toward and merge with the primary bubble, creating wrinkles (pits) on its surface. These wrinkles interact and develop into chaotic patterns during the collapse phase. Driven by Rayleigh–Taylor instability, the wrinkles evolve into finger-like structures, further intensifying the fission process of the bubble (frame 5).

In the experiments conducted in this work, we find that the aforementioned secondary cavitation occurs at higher ambient temperatures, near the moment when the main bubble reaches its maximum volume in the first oscillation cycle. This phenomenon is different from the secondary cavitation caused by rarefaction waves (Gonzalez-Avila & Ohl 2016; Supponen *et al.* 2017; Rosselló *et al.* 2023), which is independent of temperature and typically occurs after the initial expansion or collapse. In the third experiment, the estimated minimum pressure inside the bubble is approximately 47 000 Pa, much higher than in the previous two cases but significantly lower than the saturated vapour pressure (70 100 Pa) at this temperature. A detailed parametric discussion of this phenomenon will be provided in § 4.

3.2. *Maximum bubble radius*

In this section, we investigate the effect of ambient temperature on the bubble maximum radius, R_{max}, from a thermodynamic perspective. Figure 4(*a*) shows that both R_{max} and the collapse time, t_c, increase clearly with temperature. This well-documented phenomenon has been reported in previous studies (Barbaglia & Bonetto 2004; Takada *et al.* 2010; Liu *et al.* 2013). Here, we provide a more fundamental interpretation using a pressure–temperature phase diagram to map the bubble's thermodynamic state, as shown in figure 4(*b*). The solid line denotes the saturated vapour pressure, and the dashed lines represent the spinodal, which marks the boundary of metastable fluid states (Kiselev 1999). Here, it is calculated using the Peng–Robinson equation of state (Peng & Robinson 1976). Details are provided in Appendix B. When a liquid crosses the saturated line, it enters a metastable state where phase change is initiated by nucleation; when it continues to cross the spinodal line, the liquid becomes unstable and spontaneous phase separation occurs via spinodal decomposition. Before the electrical discharge, the state of water corresponds to State A, with both 23 and 90 °C experiments at their respective local hydrostatic pressures. Under transient energy deposition from an electric spark, the liquid is rapidly superheated and vaporised. We infer that the phase transition mechanism involves the liquid temperature rising to the spinodal line, denoted as State B, where the liquid becomes mechanically unstable; this state is identical for both high- and low-temperature experiments. Our interpretation is justified by the observed melting of the copper wire. This implies that the local temperature exceeded the melting point of copper (approximately 1083 °C), well above the spinodal temperature of water (approximately 323 °C at 1 atm). This view of the

https://doi.org/10.1017/jfm.2025.10838 Published online by Cambridge University Press

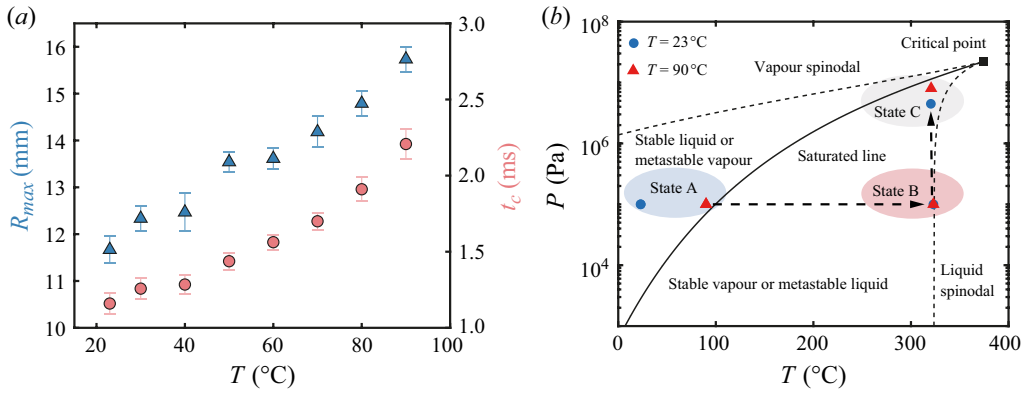


Figure 4. Effect of ambient temperature on spark-generated bubbles. (*a*) Variation of the maximum bubble radius R_{max} (blue triangles) and collapse time t_c (red circles) as functions of ambient temperature T. Error bars indicate the standard deviation. (*b*) Pressure–temperature phase diagram for spark-generated bubbles. The dashed lines denote the spinodal, representing the thermodynamic limit of stability for the vapour and liquid phases. The solid line indicates the saturated vapour pressure. Blue and red symbols mark experiments conducted at 23 and 90 °C, respectively. State A: liquid at local hydrostatic pressure and ambient temperature before discharge. State B: liquid after energy deposition, at the spinodal limit but before vaporisation. State C: the high temperature and high pressure vapour inside the initiated bubble, corresponds to the early expansion moment when the bubble reaches the same volume in both experiments.

bubble-formation mechanism has also been mentioned in previous studies (Vogel *et al.* 2005; Mohammadzadeh *et al.* 2017; Podbevšek *et al.* 2021). We nevertheless acknowledge that direct measurements of the transient temperature and pressure in the liquid, currently very challenging, would be required for definitive confirmation. As the phase transition progresses, the rapid vaporisation is confined by the inertia of the surrounding liquid, resulting in a high-temperature, high-pressure vapour bubble, denoted as State C (shown schematically). During this process, the higher ambient temperatures reduce the heat required to reach the spinodal limit, enabling a larger mass of liquid to undergo phase transition. Here, State C corresponds to the early expansion moment when the bubble reaches the same volume in both 23 and 90 °C experiments. Since more liquid is vaporised at the higher temperature, the fixed volume at State C contains a greater number of vapour moles, leading to a higher pressure and consequently a larger bubble, as shown in figure 4(*a*).

3.3. *Bubble-collapse time*

We have demonstrated that temperature significantly influences bubble collapse in figure 3. Here, we introduce the Rayleigh collapse factor, $\eta = t_c/(R_{max}\sqrt{\rho/\Delta P})$, to further quantify this effect, as depicted in figure 5(*a*). The dashed line $\eta = 0.9147$ represents the classic Rayleigh factor (Rayleigh 1917), corresponding to the collapse of a vacuum bubble under ambient pressure P_∞ in an infinite domain.

As the ambient temperature increases from 23 to 50 °C, the average Rayleigh factor initially rises from approximately 0.99 to 1.05, exceeding the theoretical value of 0.9147. As the temperature continues to rise, this trend reverses, and η declines, dropping to a value of 0.83 at $T = 90$ °C. This reflects a continuous competition between two effects across the entire temperature range, both governed primarily by the increase in internal pressure with ambient temperature. On one hand, the elevated Rayleigh factor is attributed primarily to enhanced internal resistance during collapse, caused by compression of the

https://doi.org/10.1017/jfm.2025.10838 Published online by Cambridge University Press

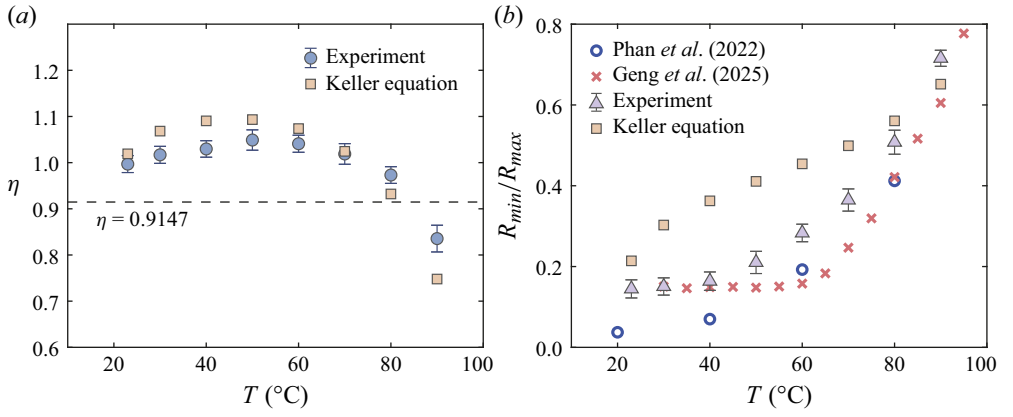


Figure 5. Effect of ambient temperature on bubble collapse. (*a*) Variation of the Rayleigh factor η versus the ambient temperature T. The circles denote the experimental data. (*b*) Variation of the non-dimensional minimum volume at the end of the first bubble-collapse stage R_{min}/R_{max} versus the dimensional ambient temperature T. The empty circles represent the results of laser-induced bubbles from Phan *et al.* (2022). The red crosses represent the results of spark-generated bubbles from Geng *et al.* (2025). The upward triangles denote the experimental data. The squares represent the results computed by the Keller equation with initial pressures of 11, 16.5, 20.7, 22.4, 28, 32, 38 and 48 kPa, which are determined by the method described in § 2.2. Error bars indicate the standard deviation.

bubble contents. This resistance slows down the collapse and prolongs the collapse duration. Two factors contribute to this. First, higher ambient temperature increases the vapour pressure inside the bubble. Second, when the condensation rate cannot keep up with the bubble-collapse velocity, some of the vapour remaining inside the bubble behaves like a compressible gas (Fujikawa & Akamatsu 1980). On the other hand, the minimum pressure of the bubble at its maximum size increases with the ambient temperature. The bubble therefore reaches the equilibrium radius earlier during the collapse, where internal and external pressures balance (Vogel, Busch & Parlitz 1996), and the collapse ends at a larger bubble radius (as shown in figure 5*b*), reducing the Rayleigh factor. Note that the bubble does not collapse to a singular point, in contrast to the classical Rayleigh description. We model this process using the Keller equation, starting from the moment of maximum expansion. The minimum bubble pressure P_{min}, estimated by (2.4), and the experimentally measured maximum radius R_{max} are used as initial conditions. Following many previous studies (Wang 2014; Liang *et al.* 2022; Rosselló *et al.* 2023), here we assume the total internal pressure to follow an adiabatic equation:

$$P_b = P_{min}\left(\frac{R_{max}}{R}\right)^{3\kappa}, \tag{3.1}$$

where κ is the polytropic exponent. Since the content of the bubble is vapour and a small amount of non-condensable gas, we set $\kappa = 1.25$ (Lee, Klaseboer & Khoo 2007; Han *et al.* 2022). The overall trend of the predictions agrees well with the experimental results with a maximum deviation of approximately 10.5 % at $T = 90\,^{\circ}\mathrm{C}$.

We also compare the normalised minimum bubble radii in figure 5(*b*). As can be seen, our experimental results exhibit a similar trend to those of laser-induced bubbles from Phan *et al.* (2022) and spark-generated bubbles from Geng *et al.* (2025). The theoretical model captures the main features in the experiments; however, we notice a more pronounced difference between experiment and calculation, especially at $T \lesssim 70\,^{\circ}\mathrm{C}$. We speculate

https://doi.org/10.1017/jfm.2025.10838 Published online by Cambridge University Press

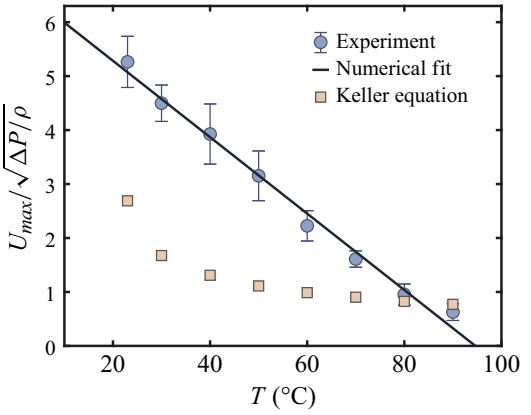


Figure 6. Variation of the non-dimensional maximum velocity during the first bubble-collapse stage, $U_{max}/\sqrt{\Delta P/\rho}$, as a function of ambient temperature T. The circles represent the experimental data and the solid line is the corresponding fitting line with a slope of −0.07 and an intercept of 6.70. The squares represent the results computed by the Keller equation using the same set-up as in § 3.3. Error bars indicate the standard deviation.

that this discrepancy is due to the theoretical framework overlooking the effects of phase change, which play a critical role in accelerating bubble collapse through condensation at the end of the collapse. Therefore, caution is warranted when applying the adiabatic approximation in cavitation bubble modelling. Despite recent progress (Zhong *et al.* 2020; Phan *et al.* 2022), a robust and generalisable phase change model applicable across a wide temperature range has yet to be established.

3.4. *Bubble-collapse velocity*

In this section, we examine the effect of ambient temperature on the bubble-collapse velocity, providing a more direct perspective on the intensity of bubble collapse. Here we focus on the maximum collapse velocity, U_{max}, which is obtained by computing the frame-to-frame time derivative of the bubble radius over the entire collapse phase and taking the maximum. The normalised maximum collapse velocity $U_{max}/\sqrt{\Delta P/\rho}$ is presented in figure 6 as a function of the ambient temperature T. Due to the limited spatiotemporal resolution of the experiments, the measured velocity should be considered a lower bound of the true collapse velocity.

The non-dimensional maximum collapse velocity decreases monotonically as the ambient temperature rises from 23 to 90 °C, dropping from approximately 5.5 to 1. The experimental data can be well fitted by a linear approximation with a slope of −0.07 and an intercept of 6.70. The root-mean-square error of this fit is 0.188. Figure 6 also shows the collapse velocity derived from the Keller equation, using the same set-up as in § 3.3. Although the theoretical results follow the same trend as our experimental observations, the predicted magnitudes are significantly underestimated, especially at temperatures below 70 °C. Again, we attribute this discrepancy to the absence of phase change in the model. In reality, vapour condensation lowers the pressure inside the bubble compared with the adiabatic approximation, thereby accelerating the bubble collapse to higher velocities. Therefore, the potential for cavitation erosion may be significantly underestimated if one uses the adiabatic approximation in their modelling. Nevertheless, agreement between the model and experiments improves at higher ambient temperatures. This suggests that the phase change effects become progressively weaker as temperature

https://doi.org/10.1017/jfm.2025.10838 Published online by Cambridge University Press

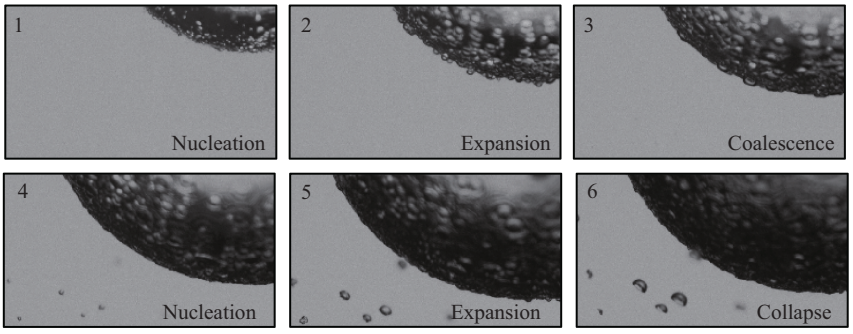


Figure 7. Experimental close-up of the evolution of secondary cavitation bubbles at 90 °C. Frames 1–3 capture the earliest instant at which secondary cavitation bubbles appear around the expanding primary bubble and subsequently coalesce with it. Frames 4–6 correspond to a later instant near maximum bubble expansion when secondary cavitation bubbles emerge at larger radial distances without noticeably perturbing the main bubble surface. The six frames occur at 0.52, 0.80, 0.99, 1.37, 2.08 and 3.08 ms. Each frame has a width of 22.3 mm.

rises, consistent with the numerical results of Phan *et al.* (2022), who demonstrated that elevated ambient temperatures suppress vapour condensation during bubble collapse. The aforementioned discussion demonstrates that increasing the ambient temperature to elevate the vapour pressure inside the bubble is an effective strategy for mitigating the intensity of bubble collapse. A similar effect can also be achieved by modifying the fluid composition. For instance, Preso *et al.* (2024*b*) showed that increasing the ammonia mass fraction in aqueous ammonia solutions yields a comparable effect.

4. Mechanism of secondary cavitation

In previous sections, we observed that the Rayleigh–Taylor instability on the bubble surface becomes particularly pronounced at high temperature, leading to bubble distortion and fission during the final stages of bubble collapse. This instability arises from initial surface perturbations caused by secondary cavitation bubbles. Figure 7 presents a series of zoomed-in images illustrating the evolution of secondary cavitation bubbles in a high-temperature environment. During the expansion phase, secondary cavitation bubbles emerge around the primary bubble and subsequently coalesce with it, leading to the formation of wrinkles or pits on the gas–liquid interface (frames 1–3). This phenomenon is particularly pronounced towards the end of the expansion phase, as nucleation sites appear farther from the main interface (frames 4–6). Once secondary cavitation triggers these perturbations, the enlarged effective surface area may enhance interfacial heat transfer. The corresponding increase in baroclinic vorticity likely amplifies the surface perturbations (Shepherd & Sturtevant 1982; Frost & Sturtevant 1986), manifested as progressively pronounced wrinkles on the bubble surface during the collapse phase. These surface distortions further enhance the Rayleigh–Taylor instability, promoting bubble fragmentation. Chen *et al.* (2024) also observed similar phenomena in spark-generated bubbles in liquid nitrogen.

The secondary cavitation phenomenon observed in this study differs from traditional secondary cavitation, which typically arises from rarefaction waves reflected at low-impedance boundaries, such as the bubble surface or free surface (Supponen *et al.* 2017; Horiba *et al.* 2020; Rosselló *et al.* 2023). The spatial distribution of this cavitation is closely associated with the area influenced by rarefaction waves, as depicted in figure 8(*a*). In our experimental set-up, this mechanism can be ruled out based on the dimensions of the

https://doi.org/10.1017/jfm.2025.10838 Published online by Cambridge University Press

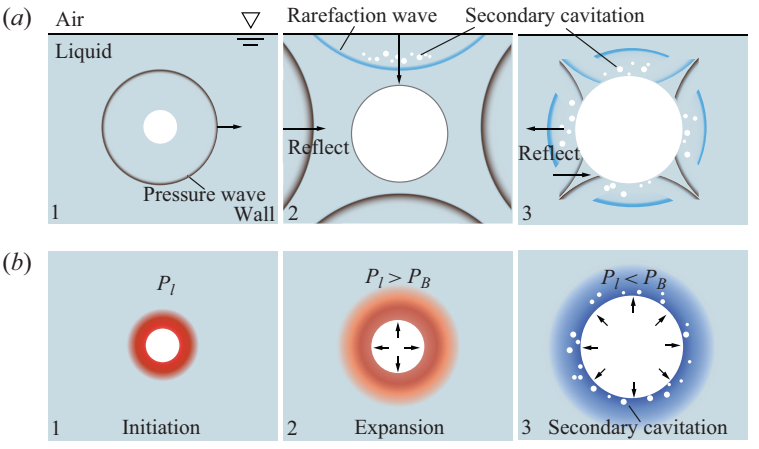


Figure 8. Schematic diagrams of two typical secondary cavitation mechanisms: (*a*) triggered by rarefaction waves and (*b*) induced by inertial expansion. P_B denotes the Blake critical pressure.

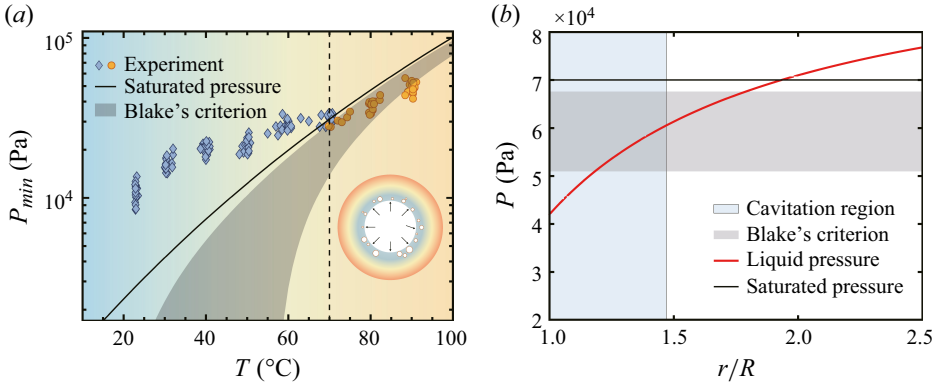


Figure 9. Mechanism of secondary cavitation. (*a*) Variation of the minimum pressure within the bubbles over the ambient temperature T. The circles denote cases where secondary cavitation occurs, while the diamonds indicate cases without secondary cavitation. (*b*) Radial distribution of liquid pressure at the moment of maximum expansion at 90 °C. The blue area indicates the cavitation region observed experimentally. The grey area indicates the Blake threshold pressure range corresponding to a microbubble radius of 2–10 μm, calculated using a surface tension of 0.061 N m^{-1}. The red solid line shows the liquid pressure $P(r, t)$ as a function of r/R, calculated from (4.3), and the black solid line denotes the saturated vapour pressure. All experiments were conducted at a discharge voltage of 200 V.

water tank and the timing of cavitation nucleation appearance. The secondary cavitation phenomenon observed here is characterised by its onset when the pressure at the bubble surface approaches the saturation pressure of the liquid medium at a specific temperature, as shown in figure 8(*b*). This perspective will be elaborated later.

Figure 9(*a*) presents the minimum bubble pressure estimated by (2.4) at different ambient temperatures. It is evident that for cases where secondary cavitation occurs (yellow circles), P_{min} consistently falls below the saturated vapour pressure (solid line). To illustrate this behaviour, we introduce Blake's criterion (Blake 1949; Neppiras & Noltingk 1951), according to which cavitation inception is expected to occur when the liquid pressure falls below a critical threshold P_B. Under isothermal conditions, P_B is given by

https://doi.org/10.1017/jfm.2025.10838 Published online by Cambridge University Press

$$P_B = P_v - \frac{4\sigma}{3R_B}, \tag{4.1}$$

where R_B is the corresponding critical bubble radius:

$$R_B = R_0\sqrt{\frac{3R_0}{2\sigma}\left(P_0 + \frac{2\sigma}{R_0}\right)}. \tag{4.2}$$

Here the subscript 0 denotes the equilibrium values for a microbubble in water, R_B is the maximum radius for which the bubble can remain in a stable equilibrium, and P_B is the corresponding minimum ambient pressure required for stability. When the ambient pressure falls below P_B, the bubble becomes unstable and grows without bound, which can be regarded as the onset of cavitation (Brennen 2014; Rosselló & Ohl 2023). On this basis, following the Bernoulli equation presented in Plesset & Prosperetti (1977), we determine the surrounding liquid pressure $P(r, t)$:

$$P(r, t) = P_\infty + \frac{R(P_l - P_\infty)}{r} + \frac{\rho R\dot{R}^2}{2r}\left[1 - \left(\frac{R}{r}\right)^3\right], \tag{4.3}$$

where r denotes the distance from the bubble centre. We plot the radial distribution of liquid pressure at the instant of maximum bubble expansion for a 90 °C experiment, as illustrated by the solid red line in figure 9(*b*). The saturated vapour pressure at this temperature is 70.1 kPa, and the experimentally observed cavitation zone (blue shading) corresponds to a critical pressure of 60.6 kPa. Taking a representative microbubble radius $R_0 = 2{-}10\,\mu$m in water (Brennen 2014) and a surface tension of 0.061 N m^{-1}, we obtain the corresponding Blake threshold P_B to be 50.9∼67.6 kPa (grey band). This interval brackets the observed critical pressure, confirming that secondary cavitation is triggered by the pressure drop in the surrounding liquid during bubble expansion. Now, we can easily understand the mechanism of secondary cavitation. Specifically, raising the ambient temperature increases the saturated vapour pressure and reduces the surface tension, effectively increasing P_B, as shown by the grey band in figure 9(*a*). The surrounding liquid pressure at the higher-temperature experiment is more prone to drop below P_B during the expansion phase, thereby facilitating nucleation of secondary cavitation.

We further investigate the influence of discharge energy on the onset of secondary cavitation. Figure 10(*a*) shows a phase diagram for the occurrence of secondary cavitation with varied discharge energy. The discharge energy E is calculated as $0.5CV_{dis}^2$ with capacitance $C = 500\,\mu$F and discharge voltage V_{dis} varied from 200 to 550 V. The critical temperature of secondary cavitation decreases from approximately 70 to 60 °C as the discharge energy increases from 10 to 75.6 J. To illustrate this trend, we compare the estimated minimum bubble pressure P_{min} at $T = 65$ °C with the Blake threshold pressure range to be 8.0∼23.1 kPa, as shown in figure 10(*b*). As the discharge energy increases, the bubble expands more rapidly, causing a further reduction in P_{min}. When the discharge energy exceeds 22.5 J, P_{min} falls below the Blake threshold range, providing the necessary conditions for secondary cavitation. Furthermore, we present the bubble-collapse time t_c, which increases with discharge energy. This suggests that the low-pressure region lasts a longer time at higher discharge energies, thereby enabling small bubbles to grow to a spatially resolvable size. These two factors explain the decrease in critical temperature with increasing discharge energy and further support that secondary cavitation is triggered by the pressure drop in the surrounding liquid during bubble expansion.

https://doi.org/10.1017/jfm.2025.10838 Published online by Cambridge University Press

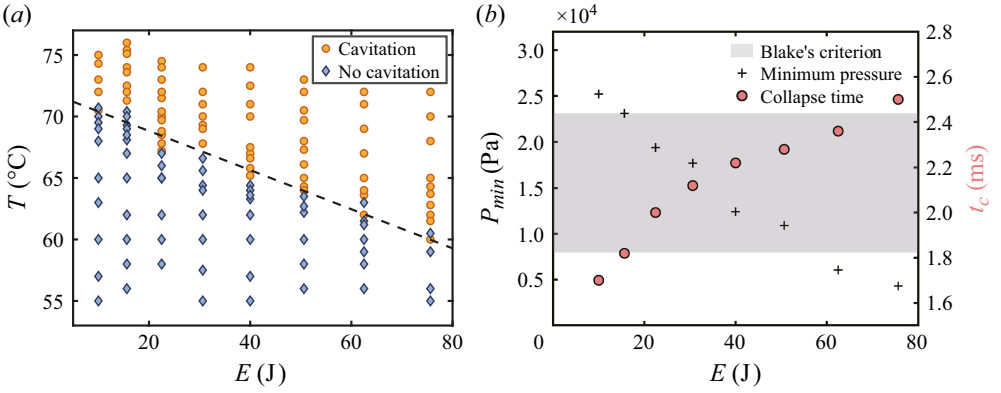


Figure 10. Influence of discharge energy on the onset of secondary cavitation. (*a*) Phase diagram for the occurrence of secondary cavitation with variation of the discharge energy E and ambient temperature. The dashed line guides the division between regimes: circles denote cases where secondary cavitation occurs, while diamonds indicate cases without secondary cavitation. The discharge energy E is calculated as $0.5CV_{dis}^2$ with capacitance $C = 500\ \mu$F and discharge voltage V_{dis} stepped from 200 to 550 V. (*b*) Minimum bubble pressure P_{min} (black crosses, left axis) and collapse time t_c (red circles, right axis) as functions of discharge energy at $T = 65\ ^\circ$C. The grey area indicates the Blake threshold pressure range corresponding to a microbubble radius of 2–10 μm, calculated using a surface tension of 0.065 N m^{-1}.

5. Bubble-collapse pattern near a rigid wall

In this section, we systematically investigate the collapse pattern of cavitation bubbles near a rigid wall under varying ambient temperatures and standoff parameters γ, defined as the ratio of the distance d between the bubble centre and the lower rigid wall to the bubble maximum radius R_{max}. We aim to reveal the dependence of bubble jetting, migration and the Kelvin impulse on the ambient temperature.

5.1. *Experimental observations*

5.1.1. *Bubble-wall interaction at the standoff distance of $\gamma \approx 2.2$*

Figure 11 illustrates the general behaviour of bubbles at $\gamma \approx 2.2$ under varying ambient temperatures. At relatively low ambient temperatures ($T = 23$ and $50\ ^\circ$C), the bubble expands (not shown here) and contracts almost spherically due to the weak constraint exerted by the wall, as shown in frames 1–2 of figures 11(*a*) and 11(*b*). However, under the secondary Bjerknes force from the wall, a jet directed toward the wall forms during the final stage of bubble collapse. As the jet travels downward, the bubble is elongated during the rebound phase (frames 4–5). During the second collapse (frame 6), the bubble is fragmented and becomes mixed with flocculent impurities, likely originating from the combustion residues of the copper alloy wire. Despite the similar general behaviours observed in the two experiments, two noteworthy observations emerge. First, the increase in temperature weakens the intensity of bubble collapse, resulting in a larger minimum radius at the end of the first cycle, consistent with the behaviour observed in a free field. Second, as the ambient temperature increases from 23 to 50 °C, the jet velocity decreases from 185 to 131 m s^{-1}.

Figure 11(*c*) illustrates representative frames from the experiment conducted at $T =$ 90 °C. Prominent wrinkles induced by secondary cavitation appear on the bubble surface, enhancing Rayleigh–Taylor instability at the end of collapse (frames 1–2). During the rebound phase, these surface wrinkles evolve into protruding bubbles (frame 3). During the second collapse, rapid contraction of the bubble's top surface generates a jet (frame 4).

https://doi.org/10.1017/jfm.2025.10838 Published online by Cambridge University Press

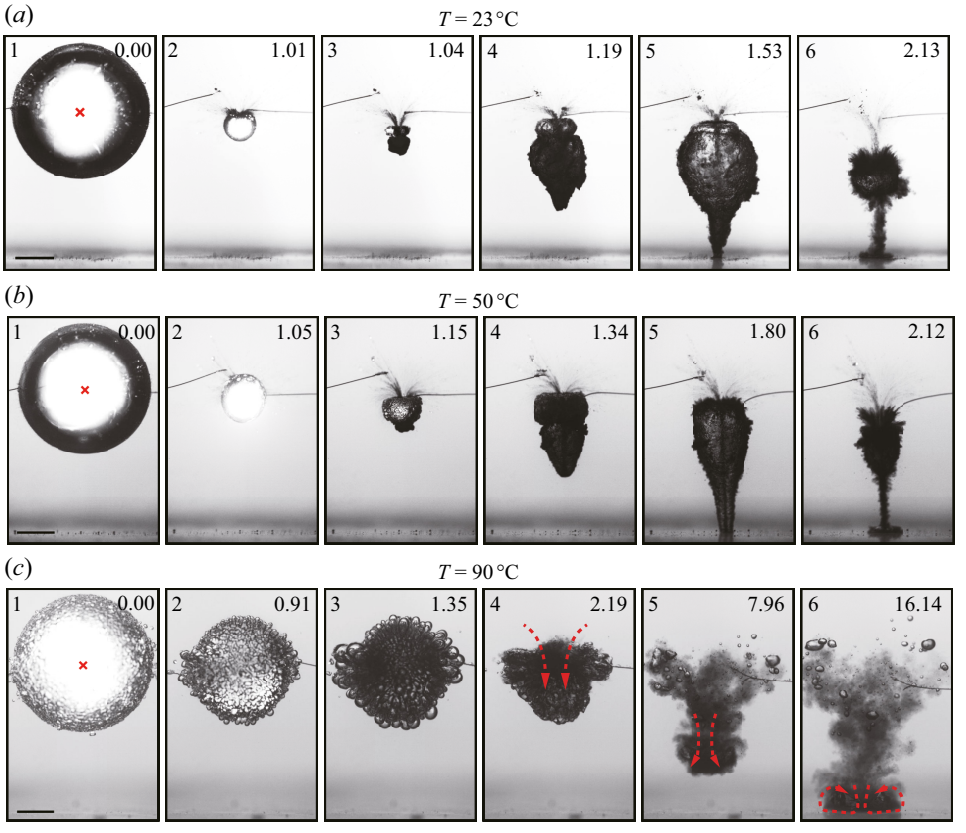


Figure 11. Selected frames show bubbles collapsing near a solid wall at three representative ambient temperatures with a standoff parameter of $\gamma \approx 2.2$. (*a*) At $T = 23\,^{\circ}\mathrm{C}$, the jet forms and penetrates almost simultaneously at minimum bubble volume. (*b*) At $T = 50\,^{\circ}\mathrm{C}$, both the minimum volume and oscillation period increase significantly. (*c*) At $T = 90\,^{\circ}\mathrm{C}$, the weak jet drives the bubbles toward the wall. Non-dimensional times are indicated in the top right corners of each frame. The time scales for non-dimensionalisation ($R_{max}\sqrt{\rho/(P_\infty - P_v)}$) are 1.77, 1.89 and 3.26 ms, respectively. The horizontal line in the bottom left corner of the first frame is 1 cm and indicates the position of the wall.

However, the jet velocity remains very low, with no significant penetration. Instead, fragmented bubbles migrate downward at approximately $1\ \mathrm{m\,s^{-1}}$ under the momentum of the jet and eventually impact the wall after a significantly long time scale (frames 5–6). As anticipated, the elevated ambient temperature substantially diminishes both the collapse intensity and jet velocity, thereby reducing the bubble's impact on the wall.

5.1.2. *Bubble–wall interaction at the standoff distance of* $\gamma \approx 0.9$

As the standoff parameter decreases, the interaction between bubble and wall strengthens. Figure 12 shows the bubble behaviours at $\gamma \approx 0.9$ under varying ambient temperatures. Experiments at 23 and 50 °C exhibit highly similar bubble collapse in non-dimensional time and scale (figure 12*a*,*b*). During collapse, liquid flow between the bubble and the lower wall is blocked, and rapid contraction in other directions drives a pronounced migration of the bubble centroid toward the wall (frames 1–3). The jet forms at an early stage of collapse and rapidly penetrates the bubble (frames 4–5). During the subsequent collapse, the bubble fully attaches to the wall (frames 6–7). Compared with the experiments at $\gamma \approx 2.2$ (§ 5.1.1), two distinctive features emerge. First, the bubble centroid

https://doi.org/10.1017/jfm.2025.10838 Published online by Cambridge University Press

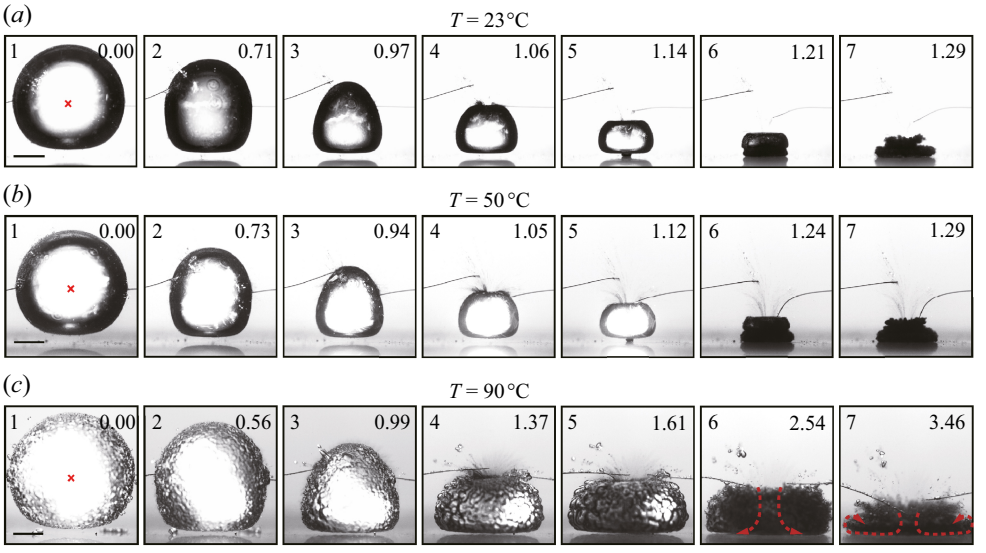


Figure 12. Selected frames show bubbles collapsing near a solid wall at three representative ambient temperatures with a standoff parameter of $\gamma \approx 0.9$. (*a*) At $T = 23\,^{\circ}\mathrm{C}$, the jet is formed early in the collapse stage and pierces the opposite wall before compressing to the bubble limit. (*b*) At $T = 50\,^{\circ}\mathrm{C}$, bubble collapse in case (*b*) is similar to (*a*) but occurs over a longer time. (*c*) At $T = 90\,^{\circ}\mathrm{C}$, the bubble surface becomes rough under the action of secondary cavitation bubbles, similar to figure 3(*c*). The time and spatial scale of bubble collapse further increase. Non-dimensional times are indicated in the top right corners of each frame. The time scales for non-dimensionalisation ($R_{max}\sqrt{\rho/(P_\infty - P_v)}$) are 1.78, 1.88 and 3.44 ms, respectively. The horizontal line in the bottom left corner of the first frame is 1 cm and indicates the position of the wall.

undergoes significant displacement during collapse, constrained by the wall. Second, the jets penetrate the bubble approximately 11.6 % and 13.2 % earlier than the final collapse, and the jet velocities in the corresponding experiments reduce to approximately 110 and 100 $\mathrm{m\,s^{-1}}$, respectively.

Figure 12(*c*) illustrates representative frames from the experiment conducted at $T = 90\,^{\circ}\mathrm{C}$. The rapid expansion of the bubble triggers secondary cavitation on both the bubble surface and the rigid wall (frames 1–3). Subsequently, a jet is formed and penetrates the bubble surface with a velocity of 23.2 $\mathrm{m\,s^{-1}}$, occurring approximately 53.4 % before the bubble reaches its minimum volume (frames 4–5). In contrast to the experiment at a larger standoff distance shown in figure 11(*c*), the bubble does not exhibit pronounced instability features, such as finger-like structures or disintegration. This can be explained as follows: the jet formation occupies a large amount of kinetic energy and thus the bubble is less compressed. The acceleration directed from gas phase towards the liquid phase is weakened, hindering the development of Rayleigh–Taylor instability. Upon jet impact, the jet fragments into droplets that collide with the bubble surface, inducing bubble rupture at the final collapse stage (frames 6–7).

5.2. *Jet speed*

In the previous section, we confirmed that the ambient temperature and standoff distance significantly influence the jet velocity. To quantify this effect, we compare the jet velocity U_{jet} under four selected ambient temperatures as a function of the standoff distance ($0.5 \lesssim \gamma \lesssim 2.5$) in figure 13(*a*). Due to the limited visibility of the bubble interior and the intense luminescence at the end of the bubble collapse, visually tracking the jet tip

https://doi.org/10.1017/jfm.2025.10838 Published online by Cambridge University Press

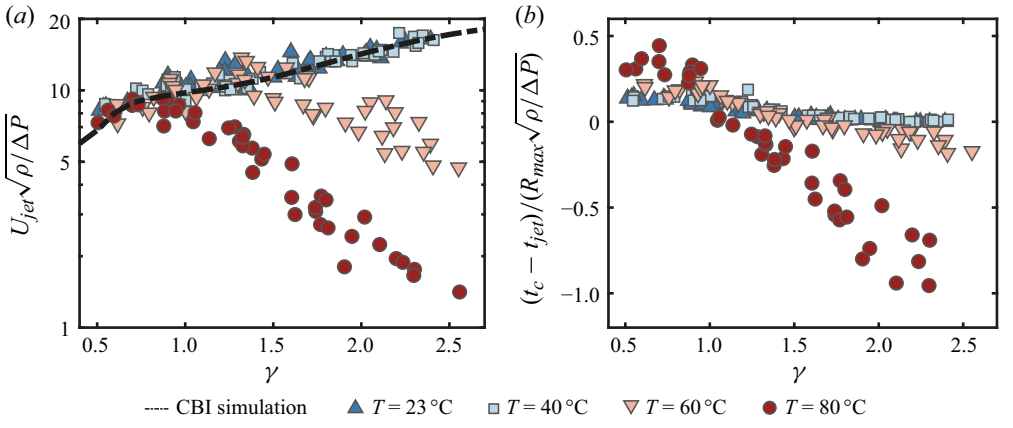


Figure 13. Dependence of jet dynamics on ambient temperature. (*a*) Dependence of the non-dimensional jet velocity $U_{jet}/\sqrt{\Delta P/\rho}$ on the standoff parameter γ. (*b*) Dependence of the non-dimensional jet impact time $(t_c - t_{jet})/(R_{max}\sqrt{\rho/\Delta P})$ on the standoff parameter γ. The shapes and colours of the markers represent various ambient temperatures, as indicated in the legend. The dashed line represents the results from CBI simulations.

is highly challenging. Therefore, we determine the jet velocity by measuring the distance and time interval between its formation and the penetration point, i.e. bubble protrusion, and normalise it by the characteristic velocity $\sqrt{\Delta P/\rho}$. Additionally, we include results obtained from compressible boundary integral (CBI) simulations (Wang 2013; Li *et al.* 2021, 2023; Yan *et al.* 2025). This method is based on weakly compressible theory (Wang & Blake 2010) that separates the flow field into two regions: the inner flow is governed by the Laplace equation, and the outer flow by the linear wave equation. Matched asymptotic expansions were employed, with perturbations performed up to second order in terms of Mach number.

Figure 13(*a*) shows experiments conducted at ambient temperatures of 23 and 40 °C. The normalised jet velocity $U_{jet}/\sqrt{\Delta P/\rho}$ increases monotonically with the standoff parameter, rising from approximately 8.2 to 17.4. It is observed that the ambient temperature has little effect on $U_{jet}/\sqrt{\Delta P/\rho}$. In addition, the results derived from the CBI simulation at room-temperature conditions show a good agreement with the experimental data.

For experiments conducted at ambient temperatures of 60 and 80 °C, the jet velocity initially increases and then decreases with increasing γ. As T rises from 60 to 80 °C, the maximum non-dimensional jet velocity decreases from approximately 13.7 at $\gamma \approx 1.32$ to 9.2 at $\gamma \approx 0.87$. The jet velocity is strongly correlated with bubble-collapse velocity at the moment of jet penetration (Philipp & Lauterborn 1998; Supponen *et al.* 2016). Specifically, the closer the jet penetration occurs to the bubble's minimum volume, the higher the resulting velocity. To illustrate the temporal relationship between jet penetration and the end of the first bubble collapse, the non-dimensional jet impact time $(t_c - t_{jet})/(R_{max}\sqrt{\rho/\Delta P})$ is presented in figure 13(*b*), where t_{jet} denotes the time when the jet tip pierces the opposite bubble wall. At lower ambient temperatures, the jet impact time decreases and gradually approaches zero as γ increases. This corresponds to the increase in jet velocity observed in figure 13(*a*). At $T = 60$ and 80 °C, jet velocity peaks when penetration occurs slightly before the minimum bubble volume. For $T = 80$ °C, if $\gamma \gtrsim 1$, jet penetration occurs during rebound, resulting in a significant reduction of jet velocity (figure 13*a*).

https://doi.org/10.1017/jfm.2025.10838 Published online by Cambridge University Press

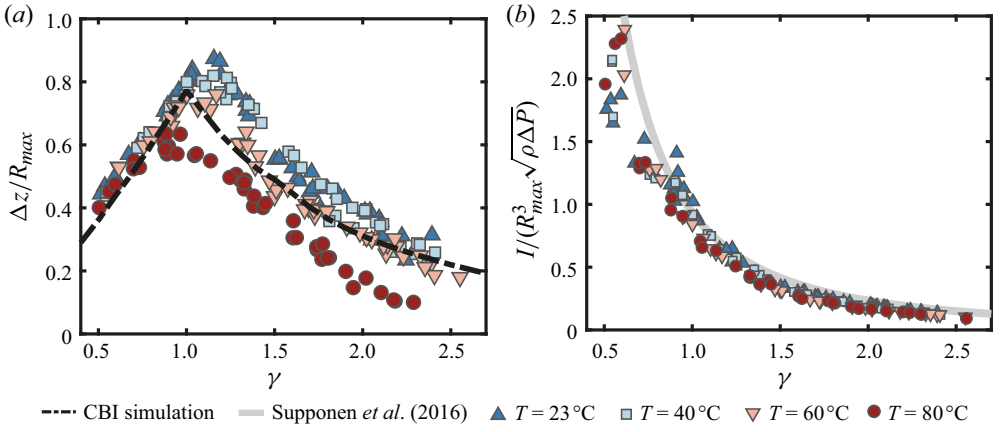


Figure 14. Bubble motion during the first cycle at different ambient temperatures. (*a*) Variation of the non-dimensional displacement of bubble centroid $\Delta z/R_{max}$ versus the standoff parameter γ. (*b*) Variation of the non-dimensional Kelvin impulse $I/(R_{max}^3\sqrt{\rho\Delta P})$ versus the standoff parameter γ. The shapes and colours of the markers represent various ambient temperatures, as indicated in the legend.

5.3. *Bubble displacement*

In this section, we investigate the effect of ambient temperature on bubble-centroid displacement, a critical parameter closely associated with the wall damage caused by jets or shock waves. Specifically, Δz is defined as the displacement from bubble inception to the end of its first collapse. Figure 14(*a*) compares the non-dimensional centroid displacement, $\Delta z/R_{max}$, across four ambient temperatures as a function of standoff parameter γ. The results obtained from CBI simulations are also included in figure 14(*a*) for comprehensive analysis.

As bubble inception approaches the rigid wall, centroid displacement initially increases and then decreases, with the transition occurring at a standoff distance of approximately $\gamma = 1$. Our CBI simulations effectively capture this feature under relatively low ambient temperatures. For $\gamma \gtrsim 1$, decreasing γ enhances the anisotropy of the pressure field induced by the wall, resulting in a more pronounced tendency for the bubble to migrate towards the wall. As γ further decreases below 1, the proximity of the boundary constrains bubble migration. Notably, under an ambient temperature of 80 °C, when the bubble is far from the boundary ($\gamma \gtrsim 1$), the centroid displacement is significantly lower than that observed in experiments conducted at lower temperatures.

To further elucidate the underlying mechanism, we introduce the Kelvin impulse I (Blake & Cerone 1982), an important concept widely used to predict the direction of bubble translation and jet formation (Blake, Leppinen & Wang 2015; Supponen *et al.* 2016; Kang & Cho 2019; Han *et al.* 2022). The Kelvin impulse is defined as

$$I = \int_0^{t_c} F \mathrm{d}t, \tag{5.1}$$

where F is the force acting vertically downward on the field, comprising two components

$$F = F_b + F_g, \tag{5.2}$$

with F_b and F_g denoting the secondary Bjerknes force and buoyancy, respectively. These forces are formulated as

https://doi.org/10.1017/jfm.2025.10838 Published online by Cambridge University Press

$$F_b = -\frac{\rho m^2}{16\pi d^2}, \tag{5.3}$$

$$F_g = \rho g V_b. \tag{5.4}$$

where g is the gravity acceleration. The source strength m is calculated using the expression $4\pi R^2 \dot{R}$, where the bubble-wall velocity $\dot{R}$ is derived from the time derivative of the bubble radius. In figure 14(*b*), we present the normalised Kelvin impulse $I/(R_{max}^3\sqrt{\rho\Delta P})$ as a function of γ. For comparison, we also include the normalised Kelvin impulse $0.934\gamma^{-2}$ (Supponen *et al.* 2016). Surprisingly, the normalised Kelvin impulse is independent of ambient temperature and agrees well with theoretical results when $\gamma > 1$. It should be noted that the dimensional Kelvin impulse decreases with ambient temperature. When $\gamma < 1$, the bubble deviates significantly from a spherical shape, placing it beyond the applicability of the Kelvin impulse theory.

In the non-dimensional framework, the centroid displacement of a cavitation bubble is influenced by its added mass. As the Kelvin impulse becomes approximately constant at the end of collapse, the migration velocity scales inversely with that added mass, which itself scales with bubble volume (Philipp & Lauterborn 1998). In our experiments, a higher ambient temperature leads to a larger minimum bubble volume. The associated increase in added mass reduces both the migration velocity and the resulting centroid displacement. This explains the dependence of the bubble displacement on ambient temperature.

6. Conclusions

This study investigated the influence of ambient temperature T (23–90 °C) on the dynamics of spark-generated cavitation bubbles at discharge energies spanning 10–75.6 J. Over four hundred experiments were conducted to quantify the thermodynamics of bubble expansion, to document the systematic attenuation of bubble collapse, and to elucidate near-wall collapse patterns. Complementary insights were provided by the Keller equation and compressible boundary integral simulations, which also helped delineate the validity range of the adiabatic approximation for the internal bubble pressure. A concise method for estimating the internal bubble pressure, in conjunction with Blake's criterion, elucidates the mechanism of secondary cavitation and its dependence on ambient temperature and discharge energy. The main findings of this study are drawn as follows.

For spherical bubbles in the free field, the maximum radius increases monotonically with ambient temperature T, as less superheat is required to approach the spinodal limit for vaporisation. However, the collapse becomes progressively weaker as T increases, as evidenced by (i) the non-dimensional minimum radius R_{min}/R_{max}, (ii) the normalised peak velocity $U_{max}/\sqrt{\Delta P/\rho}$ and (iii) the minimum internal pressure P_{min}. Increasing T from 23 to 90 °C raises R_{min}/R_{max} from 0.14 to 0.7, reduces $U_{max}/\sqrt{\Delta P/\rho}$ almost linearly from 5.5 to 1, and elevates P_{min} from 10^4 Pa to 4.9×10^4 Pa (10 J discharge). Keller-equation solutions further reveal that the adiabatic assumption for the bubble-interior pressure fails at low temperatures but remains valid at high temperatures ($\gtrsim 70$ °C).

Beyond the primary spark-generated bubble, we identify a previously unreported phenomenon that appears at ambient temperatures above 70 °C (10 J discharge): secondary cavitation nuclei emerge adjacent to the primary bubble surface and subsequently coalesce into surface wrinkles. We show that these nuclei form where the local liquid pressure drops below the Blake threshold. This pressure drop is driven by the over-expanded bubble itself, rather than by the rarefaction waves invoked in earlier studies. Quantifying the influence of discharge energy E reveals that increasing E from 10 to 75.6 J lowers the

https://doi.org/10.1017/jfm.2025.10838 Published online by Cambridge University Press

critical temperature for inception from 70 to 60 °C. Such interfacial perturbations amplify Rayleigh–Taylor instabilities and promote bubble fission during collapse.

When a bubble collapses near a rigid wall with standoff parameter $0.5 < \gamma < 2.5$, the erosion potential decreases as T rises. This trend is evidenced by the non-dimensional jet velocity $U_{jet}/\sqrt{\Delta P/\rho}$ and by the centroid displacement $\Delta z/R_{max}$. At $T = 23$ and 40 °C, $U_{jet}/\sqrt{\Delta P/\rho}$ is almost insensitive to temperature and grows monotonically with γ, consistent with earlier studies. At $T = 60$ and 80 °C, however, $U_{jet}/\sqrt{\Delta P/\rho}$ first increases with γ, reaches a maximum at an intermediate γ (where the jet penetrates slightly before the final collapse), and then declines. Although the dimensional Kelvin impulse decreases with T, the normalised Kelvin impulse collapses onto a single curve for all temperatures and obeys the classical scaling $I/(R_{max}^3\sqrt{\rho\Delta P}) \sim \gamma^{-2}$ for $\gamma \gtrsim 0.9$. The added mass of the bubble increases with T. The larger added mass lowers the migration velocity and, consequently, the centroid displacement $\Delta z/R_{max}$.

Acknowledgements. The authors thank Y. Sun, K. Lyu, T. Ding and L. Lu from Harbin Engineering University for their valuable assistance in conducting the experiments.

Funding. This work is supported by the National Natural Science Foundation of China (nos 12372239, 52525102), the Key R&D Program Project of Heilongjiang Province (JD24A002), the National Key Laboratory of Ship Structural Safety (Naklas2024ZZ004-J) and the Xplore Prize.

Declaration of interests. The authors report no conflict of interest.

Appendix A. Verification of pressure estimation within cavitation bubbles

This section quantifies the accuracy of the method used to estimate the pressure inside cavitation bubbles. As described in § 2, we approximate the bubble-radius history over an interval that encloses the instant of maximum radius with a cubic polynomial. A key adjustable parameter is the time interval employed for the fit, expressed through the non-dimensional span ratio k – the selected interval scaled by the first bubble oscillation period. To assess the sensitivity to k, we generate reference data with the Keller equation for the following parameters: initial bubble radius $R_0 = 2.228$ mm, initial internal pressure 100 P_∞, the polytropic exponent $\kappa = 1.25$, speed of sound $c_\infty = 1500\,\mathrm{m\,s^{-1}}$, liquid dynamic viscosity $\mu = 0.001$ Pa s, and surface tension coefficient $\sigma = 0.073\,\mathrm{N\,m^{-1}}$. The Keller solution yields a minimum internal pressure of 1.1×10^4 Pa. The theoretical radius curve is then sampled at the experimental temporal resolution, and (2.4) is used to recover the minimum pressure from these synthetic data. Figure 15(*a*) shows the relative error of the method as a function of k. Without added noise, the error grows monotonically with k because the cubic polynomial progressively fails to capture the true radius evolution. Real measurements are limited by spatial resolution. To examine this effect, we superimpose artificial noise of amplitudes 0.1 %, 0.5 % and 1 % of R_{max} on the clean radius history. With noise present, the relative error first decreases with fluctuations as k increases, then gradually rises and finally approaches the noise-free curve. This behaviour indicates that the fit is most vulnerable to noise at small k. Given our imaging resolution of 14 pixels per millimetre (≈0.5 % of R_{max}), we adopt $k = 0.25$, which keeps the relative error below approximately 10 %. Building on this, figure 15(*b*) further shows how the relative error scales with P_{min}. The error rises sharply as P_{min} decreases because the steeper acceleration near maximum expansion amplifies the truncation error of the cubic polynomial. Across the entire pressure range examined, the relative error remains below approximately 15 % in the present study. It should be noted that this method is most accurate when the bubble pressure is close to the ambient hydrostatic pressure. As bubble pressure drops,

https://doi.org/10.1017/jfm.2025.10838 Published online by Cambridge University Press

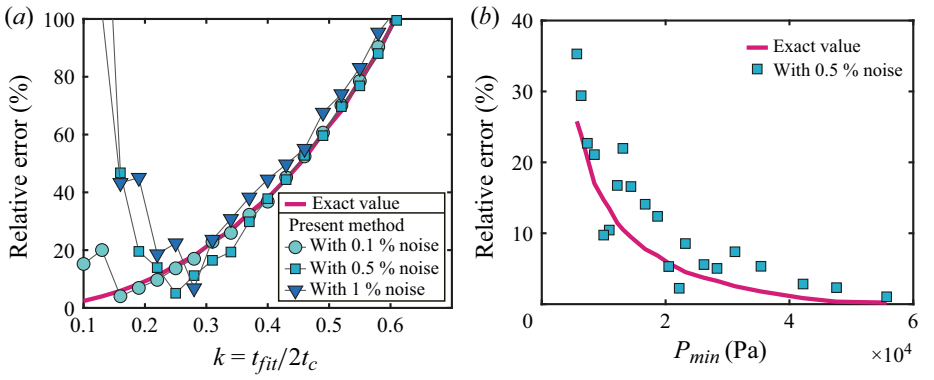


Figure 15. Accuracy assessment of the method used to estimate the pressure inside cavitation bubbles. (*a*) Relative error as a function of k. The Keller solution yields a minimum internal pressure of 1.1×10^4 Pa. The theoretical radius curve is sampled at the experimental temporal resolution, and (2.4) is used to recover the minimum pressure from these synthetic data. Solid magenta lines represent noise-free data. Circles, squares and triangles denote data with noise amplitudes of 0.1 %, 0.5 % and 1 % of R_{max} on the clean radius history. (*b*) Relative error versus P_{min}.

the uncertainty grows. If it approaches or falls below the vapour pressure, a phase change model is needed to keep the results reliable.

Appendix B. Details of spinodal determination

The spinodal line is determined from its definition, $(\partial P/\partial V_m)_T = 0$, using the Peng–Robinson equation of state (Peng & Robinson 1976), given by

$$P = \frac{\mathcal{R}T}{V_m - b} - \frac{a\alpha}{V_m^2 + 2bV_m - b^2}, \tag{B1}$$

where $\mathcal{R}$ is the universal gas constant and V_m is the molar volume. Here T is the absolute temperature in kelvin (K). The parameters a, b and α represent intermolecular attraction, molecular repulsion and temperature-dependent attraction, respectively:

$$a = 0.45724\frac{\mathcal{R}^2 T_{cr}^2}{P_{cr}^2}, \tag{B2}$$

$$b = 0.0778\frac{\mathcal{R}T_{cr}}{P_{cr}}, \tag{B3}$$

$$\alpha = \left(1 + k\left(1 - \sqrt{\frac{T}{T_{cr}}}\right)\right)^2, \tag{B4}$$

$$k \approx 0.37464 + 1.54226\omega - 0.26992\omega^2, \tag{B5}$$

with acentric factor $\omega = 0.344$ for water (Bell *et al.* 2014), and subscript cr denoting the critical point.

Appendix C. Secondary cavitation in laser-induced bubble experiments

Preliminary laser-induced cavitation experiments were conducted to test the universality of the secondary cavitation phenomenon and to exclude any influence of spark-generated

https://doi.org/10.1017/jfm.2025.10838 Published online by Cambridge University Press

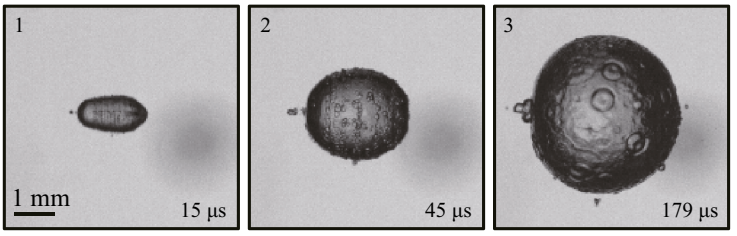


Figure 16. Laser-induced cavitation bubble in a free field at 80 °C. The bubble, initially spindle-shaped, undergoes rapid expansion, with secondary cavities nucleating around it at approximately 45 μs. By 179 μs, the coalescence of these bubbles produces pronounced surface wrinkles.

debris. The experimental set-up follows Li *et al.* (2024) and Zhao *et al.* (2025). Representative high-speed images at 80 °C (figure 16) show an initially spindle-shaped bubble that expands rapidly. Secondary cavitation nuclei appear around the primary bubble at $t = 45$ μs. By $t = 179$ μs, when the bubble attains its maximum volume, the coalesced bubbles have imprinted pronounced wrinkle-like disturbances on the interface. This reproducible sequence confirms that residual impurities from spark discharge have a negligible effect on our conclusions.

References

Barbaglia, M.O. & Bonetto, F.J. 2004 Dependence on liquid temperature and purity of light emission characteristics in single cavitation bubble luminescence. *J. Appl. Phys.* **95** (4), 1756–1759.

Beig, S.A., Aboulhasanzadeh, B. & Johnsen, E. 2018 Temperatures produced by inertially collapsing bubbles near rigid surfaces. *J. Fluid Mech.* **852**, 105–125.

Bell, I.H., Wronski, J., Quoilin, S. & Lemort, V. 2014 Pure and pseudo-pure fluid thermophysical property evaluation and the open-source thermophysical property library coolprop. *Ind. Engng Chem. Res.* **53** (6), 2498–2508.

Blake, F.G. 1949 *Onset of Cavitation in Liquids*. Harvard University.

Blake, J.R. & Cerone, P. 1982 A note on the impulse due to a vapour bubble near a boundary. *ANZIAM J.* **23** (4), 383–393.

Blake, J.R., Leppinen, D.M. & Wang, Q. 2015 Cavitation and bubble dynamics: the Kelvin impulse and its applications. *Interface Focus* **5** (5), 20150017.

Brennen, C.E. 2002 Fission of collapsing cavitation bubbles. *J. Fluid Mech.* **472**, 153–166.

Brennen, C.E. 2014 *Cavitation and Bubble Dynamics*. Cambridge University Press.

Brenner, M.P., Hilgenfeldt, S. & Lohse, D. 2002 Single-bubble sonoluminescence. *Rev. Mod. Phys.* **74** (2), 425.

Caupin, F. & Herbert, E. 2006 Cavitation in water: a review. *C. R. Phys.* **7** (9-10), 1000–1017.

Chen, J., Chen, T., Geng, H., Huang, B. & Cao, Z. 2024 Investigation on dynamic characteristics and thermal effects of single cavitation bubble in liquid nitrogen. *Phys. Fluids* **36** (2), 023325.

Cui, P., Zhang, A.-M., Wang, S. & Khoo, B.C. 2018 Ice breaking by a collapsing bubble. *J. Fluid Mech.* **841**, 287–309.

Dular, M. 2016 Hydrodynamic cavitation damage in water at elevated temperatures. *Wear* **346**, 78–86.

Dular, M. & Coutier-Delgosha, O. 2013 Thermodynamic effects during growth and collapse of a single cavitation bubble. *J. Fluid Mech.* **736**, 44–66.

Dular, M. & Petkovšek, M. 2018 Cavitation erosion in liquid nitrogen. *Wear* **400**, 111–118.

Frost, D. & Sturtevant, B. 1986 Effects of ambient pressure on the instability of a liquid boiling explosively at the superheat limit. *J. Heat Transfer* **108**, 418–424.

Fujikawa, S. & Akamatsu, T. 1980 Effects of the non-equilibrium condensation of vapour on the pressure wave produced by the collapse of a bubble in a liquid. *J. Fluid Mech.* **97** (3), 481–512.

Geng, H., Chen, T., Chen, J., Huang, B. & Wang, G. 2025 Temperature effects on single cavitation bubble dynamics under the free field condition: experimental and theoretical investigations on water. *Ultrason. Sonochem.* **120**, 107520.

Gonzalez-Avila, S.R. & Ohl, C.-D. 2016 Fragmentation of acoustically levitating droplets by laser-induced cavitation bubbles. *J. Fluid Mech.* **805**, 551–576.

https://doi.org/10.1017/jfm.2025.10838 Published online by Cambridge University Press

HAN, L., YAN, S. & LI, S. 2024 Theoretical investigation of spherical bubble dynamics in high Mach number regimes. *J. Mar. Sci. Appl.* **23** (1), 39–48.
HAN, R., ZHANG, A.-M., TAN, S. & LI, S. 2022 Interaction of cavitation bubbles with the interface of two immiscible fluids on multiple time scales. *J. Fluid Mech.* **932**, A8.
HORIBA, T., OGASAWARA, T. & TAKAHIRA, H. 2020 Cavitation inception pressure and bubble cloud formation due to the backscattering of high-intensity focused ultrasound from a laser-induced bubble. *J. Acoust. Soc. Am.* **147** (2), 1207–1217.
KANG, Y.J. & CHO, Y. 2019 Gravity-capillary jet-like surface waves generated by an underwater bubble. *J. Fluid Mech.* **866**, 841–864.
KELLER, J.B. & MIKSIS, M. 1980 Bubble oscillations of large amplitude. *J. Acoust. Soc. Am.* **68** (2), 628–633.
KISELEV, S.B. 1999 Kinetic boundary of metastable states in superheated and stretched liquids. *Physica A* **269** (2–4), 252–268.
LECHNER, C., LAUTERBORN, W., KOCH, M. & METTIN, R. 2019 Fast, thin jets from bubbles expanding and collapsing in extreme vicinity to a solid boundary: a numerical study. *Phys. Rev. Fluids* **4** (2), 021601.
LEE, M., KLASEBOER, E. & KHOO, B.C. 2007 On the boundary integral method for the rebounding bubble. *J. Fluid Mech.* **570**, 407–429.
LI, S., SAADE, Y., VAN DER MEER, D. & LOHSE, D. 2021 Comparison of boundary integral and volume-of-fluid methods for compressible bubble dynamics. *Intl J. Multiphase Flow* **145**, 103834.
LI, S., ZHANG, A.-M. & HAN, R. 2023 3D model for inertial cavitation bubble dynamics in binary immiscible fluids. *J. Comput. Phys.* **494**, 112508.
LI, S., ZHAO, Z., ZHANG, A.-M. & HAN, R. 2024 Cavitation bubble dynamics inside a droplet suspended in a different host fluid. *J. Fluid Mech.* **979**, A47.
LIANG, X.X., LINZ, N., FREIDANK, S., PALTAUF, G. & VOGEL, A. 2022 Comprehensive analysis of spherical bubble oscillations and shock wave emission in laser-induced cavitation. *J. Fluid Mech.* **940**, A5.
LIU, X.-M., LONG, Z., HE, J., LI, B.-B., LIU, X.-H., ZHAO, J.-Y., LU, J. & NI, X.-W. 2013 Experimental study of temperature effect on the growth and collapse of cavitation bubbles near a rigid boundary. *Optoelectron. Lett.* **9** (4), 317–320.
MOHAMMADZADEH, M., GONZALEZ-AVILA, S.R., LIU, K., WANG, Q.J. & OHL, C.-D. 2017 Synthetic jet generation by high-frequency cavitation. *J. Fluid Mech.* **823**, R3.
NEPPIRAS, E.A. & NOLTINGK, B.E. 1951 Cavitation produced by ultrasonics: theoretical conditions for the onset of cavitation. *Proc. Phys. Soc. B* **64** (12), 1032.
PENG, D.-Y. & ROBINSON, D.B. 1976 A new two-constant equation of state. *Ind. Engng Chem. Fundam.* **15** (1), 59–64.
PHAN, T.H., KADIVAR, E., NGUYEN, V.T., EL MOCTAR, O. & PARK, W.G. 2022 Thermodynamic effects on single cavitation bubble dynamics under various ambient temperature conditions. *Phys. Fluids* **34** (2), 023318.
PHILIPP, A. & LAUTERBORN, W. 1998 Cavitation erosion by single laser-produced bubbles. *J. Fluid Mech.* **361**, 75–116.
PLESSET, M.S. 1972 Temperature effects in cavitation damage. *J. Basic Engng* **94** (3), 559–563.
PLESSET, M.S. & PROSPERETTI, A. 1977 Bubble dynamics and cavitation. *Annu. Rev. Fluid Mech.* **9** (1), 145–185.
PODBEVŠEK, D., LOKAR, Ž., PODOBNIKAR, J., PETKOVŠEK, R. & DULAR, M. 2021 Experimental evaluation of methodologies for single transient cavitation bubble generation in liquids. *Exp. Fluids* **62**, 1–28.
PRESO, D.B., FUSTER, D., SIEBER, A.B. & FARHAT, M. 2024*a* Effects of non-condensable gas on laser-induced cavitation bubbles. arXiv preprint arXiv: 2401.15421.
PRESO, D.B., FUSTER, D., SIEBER, A.B., OBRESCHKOW, D. & FARHAT, M. 2024*b* Vapor compression and energy dissipation in a collapsing laser-induced bubble. *Phys. Fluids* **36** (3), 033342.
PUTTERMAN, S.J. & WENINGER, K.R. 2000 Sonoluminescence: how bubbles turn sound into light. *Annu. Rev. Fluid. Mech.* **32** (1), 445–476.
RAYLEIGH, LORD. 1917 On the pressure developed in a liquid during the collapse of a spherical cavity. *Lond. Edin. Dublin Phil. Mag. J. Sci.* **34** (200), 94–98.
REESE, H., SCHÄDEL, R., REUTER, F. & OHL, C.-D. 2022 Microscopic pumping of viscous liquids with single cavitation bubbles. *J. Fluid Mech.* **944**, A17.
REUTER, F., DEITER, C. & OHL, C.-D. 2022 Cavitation erosion by shockwave self-focusing of a single bubble. *Ultrason. Sonochem.* **90**, 106131.
ROSSELLÓ, J.M. & OHL, C.-D. 2023 Clean production and characterization of nanobubbles using laser energy deposition. *Ultrason. Sonochem.* **94**, 106321.

https://doi.org/10.1017/jfm.2025.10838 Published online by Cambridge University Press

ROSSELLÓ, J.M., REESE, H., RAMAN, K.A. & OHL, C.-D. 2023 Bubble nucleation and jetting inside a millimetric droplet. *J. Fluid Mech.* **968**, A19.

SEDDON, J.R.T., KOOIJ, E.S., POELSEMA, B., ZANDVLIET, H.J.W. & LOHSE, D. 2011 Surface bubble nucleation stability. *Phys. Rev. Lett.* **106** (5), 056101.

SHEPHERD, J.E. & STURTEVANT, B. 1982 Rapid evaporation at the superheat limit. *J. Fluid Mech.* **121**, 379–402.

SUN, C., CAN, E., DIJKINK, R., LOHSE, D. & PROSPERETTI, A. 2009 Growth and collapse of a vapour bubble in a microtube: the role of thermal effects. *J. Fluid Mech.* **632**, 5–16.

SUPPONEN, O., OBRESCHKOW, D., KOBEL, P., TINGUELY, M., DORSAZ, N. & FARHAT, M. 2017 Shock waves from nonspherical cavitation bubbles. *Phys. Rev. Fluids* **2** (9), 093601.

SUPPONEN, O., OBRESCHKOW, D., TINGUELY, M., KOBEL, P., DORSAZ, N. & FARHAT, M. 2016 Scaling laws for jets of single cavitation bubbles. *J. Fluid Mech.* **802**, 263–293.

TAKADA, N., NAKANO, T. & SASAKI, K. 2010 Formation of cavitation-induced pits on target surface in liquid-phase laser ablation. *Appl. Phys. A* **101**, 255–258.

TURANGAN, C.K., ONG, G.P., KLASEBOER, E. & KHOO, B.C. 2006 Experimental and numerical study of transient bubble-elastic membrane interaction. *J. Appl. Phys.* **100** (5), 054910.

VOGEL, A., BUSCH, S. & PARLITZ, U. 1996 Shock wave emission and cavitation bubble generation by picosecond and nanosecond optical breakdown in water. *J. Acoust. Soc. Am.* **100** (1), 148–165.

VOGEL, A., NOACK, J., HÜTTMAN, G. & PALTAUF, G. 2005 Mechanisms of femtosecond laser nanosurgery of cells and tissues. *Appl. Phys. B* **81** (8), 1015–1047.

WANG, Q. 2013 Non-spherical bubble dynamics of underwater explosions in a compressible fluid. *Phys. Fluids* **25** (7), 072104.

WANG, Q. 2014 Multi-oscillations of a bubble in a compressible liquid near a rigid boundary. *J. Fluid Mech.* **745**, 509–536.

WANG, Q. 2016 Local energy of a bubble system and its loss due to acoustic radiation. *J. Fluid Mech.* **797**, 201–230.

WANG, Q. & BLAKE, J.R. 2010 Non-spherical bubble dynamics in a compressible liquid. Part 1. Travelling acoustic wave. *J. Fluid Mech.* **659**, 191–224.

WEI, A., YU, L., QIU, L. & ZHANG, X. 2022 Cavitation in cryogenic fluids: a critical research review. *Phys. Fluids* **34** (10), 101303.

WU, H., ZHENG, H., LI, Y., OHL, C.-D., YU, H. & LI, D. 2021 Effects of surface tension on the dynamics of a single micro bubble near a rigid wall in an ultrasonic field. *Ultrason. Sonochem.* **78**, 105735.

YAN, S., CHEN, Y., LYU, K., QIN, H., ZHANG, A.-M. & LI, S. 2025 Numerical and experimental benchmark study of nonspherical cavitation bubble dynamics near a rigid wall. *Appl. Ocean Res.* **154**, 104423.

ZENG, Q., GONZALEZ-AVILA, S.R., DIJKINK, R., KOUKOUVINIS, P., GAVAISES, M. & OHL, C.-D. 2018 Wall shear stress from jetting cavitation bubbles. *J. Fluid Mech.* **846**, 341–355.

ZHANG, A.-M., LI, S.-M., XU, R.-Z., PEI, S.-C., LI, S. & LIU, Y.-L. 2024 A theoretical model for compressible bubble dynamics considering phase transition and migration. *J. Fluid Mech.* **999**, A58.

ZHAO, Z., LI, S., XIONG, C., CUI, P., WANG, S. & ZHANG, A.-M. 2025 New insights into the cavitation erosion by bubble collapse at moderate stand-off distances. *J. Fluid Mech.* **1015**, A33.

ZHONG, X., ESHRAGHI, J., VLACHOS, P., DABIRI, S. & ARDEKANI, A.M. 2020 A model for a laser-induced cavitation bubble. *Intl J. Multiphase Flow* **132**, 103433.

https://doi.org/10.1017/jfm.2025.10838 Published online by Cambridge University Press